# Tunable inverse topological heterostructure utilizing $(Bi_{1-x}In_x)_2Se_3$ and multi-channel weak-antilocalization effect

Matthew Brahlek[1†#], Nikesh Koirala[1†], Jianpeng Liu[1], Tahir I. Yusufaly[1], Maryam Salehi[2], Myung-Geun Han[3], Yimei Zhu[3], David Vanderbilt[1], and Seongshik Oh[1,*]

[1]Department of Physics & Astronomy, Rutgers, The State University of New Jersey, Piscataway, New Jersey 08854, U.S.A.

[2]Department of Materials Science and Engineering, Rutgers, The State University of New Jersey, Piscataway, New Jersey 08854, U.S.A.

[3]Condensed Matter Physics & Materials Science, Brookhaven National Lab, Upton, NY 11973, U.S.A.

*Correspondence should be addressed to ohsean@physics.rutgers.edu

[†]These authors contributed equally to this work

[#]Present address: Department of Materials Science and Engineering, Pennsylvania State University, University Park, Pennsylvania 16802, U.S.A.

**Contents:**

- **A:** Experimental methods
- **B:** Computational methods
- **C**: Weak anti-localization: numerical fitting

# A: Experimental methods

All samples were grown using 10 mm × 10 mm $c$-plane $Al_2O_3$ substrates. The first $Bi_2Se_3$ layer was grown according to the two-step growth method developed at Rutgers University where the first 3 QL was grown at 135°C, which was followed by slowly annealing the sample to 300°C, where the subsequent 27 QL of $Bi_2Se_3$ layers were grown. Once the first $Bi_2Se_3$ layer finished growth, the $In_2Se_3$ of the specified thickness was grown, followed by the remaining $Bi_2Se_3$ layer. $Bi_2Se_3$ (lattice constant of 4.14 Å) and $In_2Se_3$ (4.00 Å) both fully relax within the first QL of heteroepitaxy. All the samples were then capped by 50 QL of $In_2Se_3$ which stabilized the films during exposure to atmosphere. For the samples with $(Bi_{1-x}In_x)_2Se_3$ as the barrier layer, the same basic recipe was used. The Bi and In cell temperatures were adjusted such that when opened together the resulting film gave the concentration that was sought. All the concentrations were checked by a combination of ex situ Rutherford back scattering spectroscopy and in situ quartz crystal microbalance measurements, and the results were within ±1% of the target values.
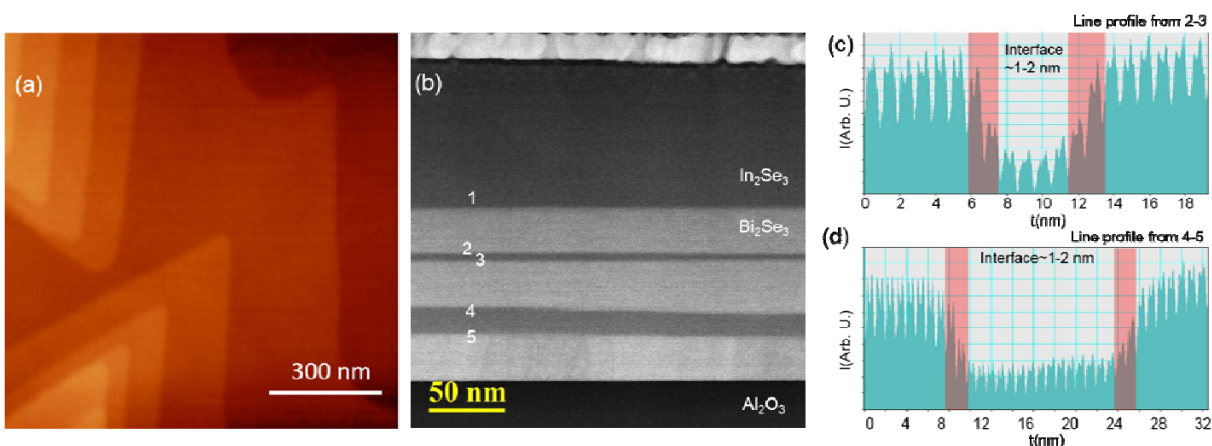


**Figure S1.** (a) 1 μm × 1 μm atomic force microscopy image showing the surface morphology. (b), Wide angle high-resolution high-angle annular dark-field scanning transmission electron microscopy for a 30-20-30-5-30 QL film. (c-d) Electron energy loss spectroscopy profiles taken across the interfaces in (b) as indicated.

TEM sample preparation was carried out with focused-ion beam (FIB) technique using 5 keV $Ga^+$ ions. A JEOL ARM 200CF equipped with a cold field-emission gun and double-spherical aberration correctors operated at 200 kV was used for high-angle annular dark-field (HAADF) scanning transmission electron microscopy (STEM) with the collection angles ranging from 68 to 280 mrad. As shown by atomic force microscopy and HAADF STEM in Fig. S1 (a-b), the interfaces of the films are flat with well-defined interfaces. Some Bi-In interdiffusion may occur but electron energy loss spectroscopy in Fig. S1 (c-d) shows it to be mostly confined to the first QL of the interface [1].

As shown in Fig. S2, transport measurements were carried out at 1.5 K using the standard 4-point Van der Pauw lead geometry, and the magnetic field was applied perpendicular to the films' surface. Both $Bi_2Se_3$ layers were equally contacted by physically pressing ~mm sized indium contacts into the film. The raw data was symmetrized to remove any odd component from $R_{xx}$ and any even component from $R_{xy}$. The carrier density and mobility of the films ranged between 3-7 × $10^{13}$ /cm$^2$ and 500-1000 cm$^2$/Vs, and there was no correlation between the transport data and the value of $\tilde{A}$. From the WAL fitting, $l_\phi$ ranged between 50-100 nm and also showed little correlation with the other transport data or $\tilde{A}$. The temperature

dependence of resistivity for all samples showed typical monotonic decreasing behavior with decreasing temperature, which is typical of a metal. $\tilde{A}$ was independent of temperature below ~20 K, above which deviation occurred as thermal effect suppresses the WAL signal.
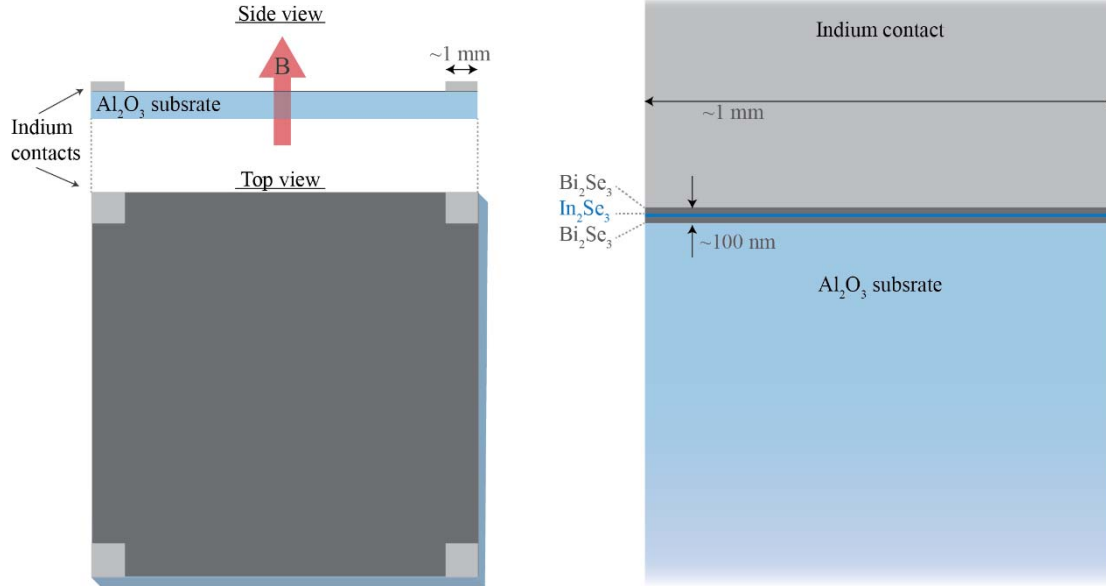


**Figure S2.** Schematic of the experimental setup where the films were grown on 10 mm × 10 mm square substrates, and electrical contact was made using millimeter size indium pads in the Van der Pauw geometry. The blow up on the right shows the scale of the thin film relative to the substrate and contact size (i.e. ~100 nm film relative to millimeter substrate thickness and contact area). The huge aspect ratio (over tens of thousands) between the lateral contact dimensions and the film thickness allows uniform current flow through both the top and bottom TI layers.

## B: Computational methods

### B1. Tunneling between topological interface states

The tunneling between the topological surface states (TSS) in $Bi_2Se_3$-$In_2Se_3$-$Bi_2Se_3$ heterostructures was studied based on density-functional theory (DFT) [2,3]. Calculations on bulk $Bi_2Se_3$ and $In_2Se_3$ were first performed using the Quantum ESPRESSO package [4], with the generalized gradient approximation (GGA) [5] to the exchange-correlation functional and fully relativistic norm-conserving pseudopotentials. The Brillouin zone (BZ) was sampled on an 8×8×8 Monkhorst-Pack [6] $k$ mesh, with an energy cutoff of 55 Ry (1 Ry ≈ 13.6 eV) for $Bi_2Se_3$ and 65 Ry for $In_2Se_3$. The first-principles output was fed into the Wannier90 package to produce Wannier functions (WFs) and to generate a realistic tight-binding (TB) model defined in the chosen Wannier basis [7,8]. 30 Wannier functions were constructed for $Bi_2Se_3$, including all the valence $p$ orbitals, while four extra In $5s$ orbitals were included for $In_2Se_3$. Both models were constructed in such a way that they exactly reproduce the first-principles bandstructures within a certain energy range, spanning from 3 eV below to 3 eV above the Fermi level.

The supercells including a $Bi_2Se_3$-$In_2Se_3$ interface can be constructed based on the bulk TB models. First, the Wannier-based model Hamiltonians for bulk $Bi_2Se_3$ and $In_2Se_3$, denoted as $H_1$ and $H_2$, were extrapolated to $N_1$ QL and $N_2$ QL slabs stacked in the [111] direction with open boundary conditions. These two isolated slabs were connected together in such a way that all the first-neighbor hopping (here referring to hopping terms between nearest-neighbor QLs) across the interface were taken as the average

value of the corresponding hopping terms in the $Bi_2Se_3$ and $In_2Se_3$ bulk TB models. Then the periodic boundary condition was applied to the $(N_1 + N_2)$-QL slab to make it a periodic supercell. The total thickness of $Bi_2Se_3$ and $In_2Se_3$ was fixed to be $N_1 + N_2 = 12$ QLs, and the thickness of $In_2Se_3$ was varied from $N_2 = 1$ to 6 QLs (for the data shown in Fig. 2(h) of the main text, $N_1 + N_2 = 16$ QLs with $N_2 = 8$). Working in the Wannier basis allows for the thickness of $In_2Se_3$ in the heterostructure to be highly tunable, and the computational cost is negligible compared with a fully self-consistent interface calculation.

In implementing this procedure, two issues need to be addressed. First, at the bulk level, standard DFT tends to underestimate the energy of the In $5s$ level. Because the lowest conduction band and highest valence band of $In_2Se_3$ are dominated by In $5s$ and Se $4p$ orbitals respectively, DFT predicts a smaller band gap compared with experiment [9]. Here a corrective treatment was adopted as described in ref. [9], which involves applying a +0.79 eV rigid shift (taken from many-body GW calculations) to the four In $5s$ levels in the 34-band model for $In_2Se_3$, leaving all the other matrix elements unchanged.

Another issue is the band offset between the two bulk materials. Initially the zeroes of energy of the Wannierized tight-binding models for $Bi_2Se_3$ and $In_2Se_3$ are inherited from the respective bulk DFT bulk calculations, but as is well known, these are largely arbitrary, as they depend on irrelevant details such as the choice of pseudopotentials. To address this issue, the alignment method based on surface work functions [10] was adopted by carrying out self-consistent surface slab calculations on $Bi_2Se_3$ and $In_2Se_3$ slabs individually, from which the difference between the average electrostatic potential energy deep in the bulk and in the vacuum was evaluated for each material. This was done by computing the macroscopic-averaged electrostatic potential $\overline{\phantom{V}}$ from the microscopic potential $\phantom{as:}$ as: $\overline{\phantom{V}}$

$\phantom{}$, where $c$ and $A$ are the cell height (size of a QL) and basal area respectively. For these calculations, a 3-QL slab was used, and slabs were chosen to be separated from
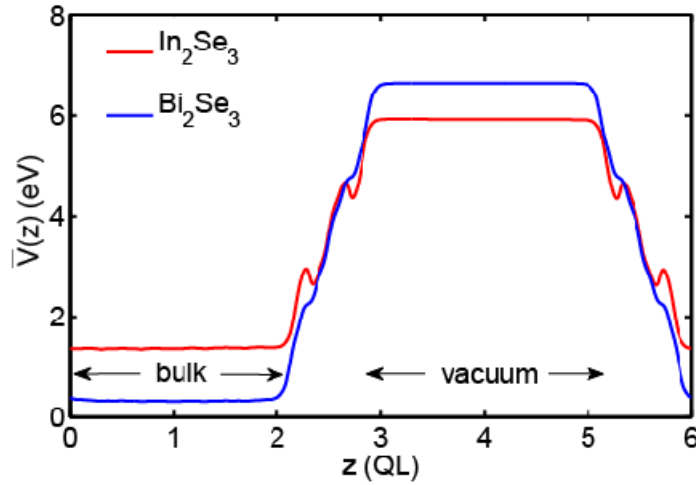


**Figure S3**. The macroscopic average of the electrostatic potentials of $Bi_2Se_3$ and $In_2Se_3$ slabs.

each other by a vacuum space of 2.9 nm. The macroscopic averages of the electrostatic potentials are plotted in Fig. S3. Note that due to the non-polar crystal structure and the homogeneous nature of the vacuum $\overline{\phantom{V}}$ remains constant both deep in the bulk and in vacuum. Aligning the vacuum levels, it was concluded that the relative shift between the average electrostatic potential in bulk $Bi_2Se_3$ vs $In_2Se_3$

is     –         . Therefore, the arbitrariness in the energy zeroes can be removed by shifting all the Kohn-Sham eigenenergies of $In_2Se_3$ using          .

With the GW correction to In $5s$ levels and the shift      on all the $In_2Se_3$ on-site energies, the interface model has been well constructed. The eigenvalues were then calculated in the $(k_x, k_y)$ plane, setting $k_z = 0$. If the TSS do not interact, a doubly degenerate gapless Dirac cone around $\Gamma$ ($k_x = 0, k_y = 0$) is expected, but the energy spectrum should become gapped when a tunneling interaction is allowed. Therefore, the band gap at $\Gamma$, denoted as $\Delta(\Gamma)$, should provide a measure reflecting the tunneling amplitude between the TSSs. As shown in Fig. 2(d) in the main text, $\Delta(\Gamma)$ was found to drop exponentially as the thickness of the $In_2Se_3$ layer increases. Setting 0.05 eV as a threshold below which the tunneling between the TSS is considered as negligible, the corresponding critical thickness $t_c$ is about ~2.6 QLs, which agrees well with experimental data.

One may also be interested in the real-space distribution of the interface states, which can be easily calculated using the interface model described above. The following quantity is introduced as a weight of the real space density of the interface states around the Fermi level [11]   z:
$\underline{\hspace{5cm}}$          where          and          are the components of the Bloch states at $\Gamma$ projected onto the Wannier functions centered at  , and the superscripts    and    refer to the highest occupied and lowest unoccupied states respectively. If the Fermi level lies slightly above the conduction band minimum (CBM) at $\Gamma$,          measures the   -dependence of the charge density averaged over the   - plane around the Fermi level.          is denoted as the real space density of the states (RDOS) in the main text, as shown in Fig. 2(e-h).
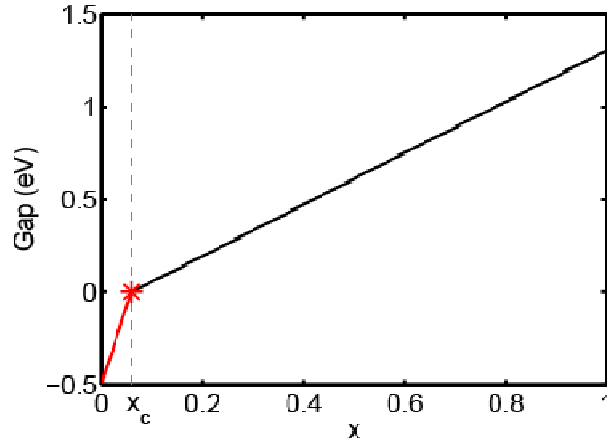


**Figure S4.** The bulk gap of $(Bi_{1-x}In_x)_2Se_3$ at $\Gamma$ from linear interpolations. The asterisk marks the critical point. A negative gap (red segment) indicates a topological band inversion.

## B2. Band alignment

The position of the $In_2Se_3$ conduction band minimum (CBM) and valence band maximum (VBM) with respect to the $Bi_2Se_3$ VBM can also be determined from the above self-consistent slab calculations. It turns out that the $In_2Se_3$ CBM and VBM at $\Gamma$ (including the +0.79 eV correction on In $5s$ levels) are 1.286 eV above and -0.018 eV below the $Bi_2Se_3$ VBM respectively. Such information is useful in evaluating the band alignment in $(Bi_{1-x}In_x)_2Se_3$. However, the CBM and VBM positions for different $x$ values cannot be evaluated simply by linearly interpolating the two end points ($x = 0\%$ and $100\%$), because a linear gap-closure picture does not apply to $(Bi_{1-x}In_x)_2Se_3$ over the entire $x$ interval, the bulk band gap vanishes at

5

very low In composition as a result of the In clustering tendency and the presence of In $5s$ orbitals [9,12,13]. In order to treat the band alignment in $(Bi_{1-x}In_x)_2Se_3$ better, the position of the 3D Dirac point at criticality was also extracted from ref. [9], which is 0.106 eV above the VBM of $Bi_2Se_3$. Even though the theoretical critical point of $(Bi_{1-x}In_x)_2Se_3$ ($x_c \approx 16.7\%$) is higher than the experimental value ($x_c \approx 6\%$ [13], $x_c \approx 4-7\%$ [12]), here it is assumed that the theoretical shift of the 3D Dirac point with respect to the $Bi_2Se_3$ VBM at criticality also applies to the experimental situation. Namely, it is assumed that the 3D Dirac point is 0.106 eV above the $Bi_2Se_3$ VBM at $x = 6\%$.

**Table S2.** Band alignment of $(Bi_{1-x}In_x)_2Se_3$

| $x$ | 0 | 6% | 20% | 60% | 100% |
|---|---|---|---|---|---|
| VBM (eV) | 0 | 0.106 | 0.088 | 0.035 | −0.018 |
| CBM (eV) | 0.490 | 0.106 | 0.280 | 0.786 | 1.286 |

Using the positions of the CBM and VBM at 3 different $x$ values as specified above ($x = 0\%$, 6% and 100%), the CBM and VBM for any other $x$ can be obtained from two separate linear interpolations in the left and right intervals partitioned by $x_c$. Under such an approximation, the gap vs $x$ consists of two linear curves with different slopes, as shown in Fig. S4, instead of a single straight line as predicted by a simple linear-gap-closure picture.

   Table S2 and Fig. S5 show the alignments of the CBM and VBM of $(Bi_{1-x}In_x)_2Se_3$ with respect to the VBM of $Bi_2Se_3$ at different $x$. When $x$ is 20%, the CBM of $(Bi_{1-x}In_x)_2Se_3$ is below that of $Bi_2Se_3$, which means that in a realistic case in which the Fermi level is slightly above the CBM of $Bi_2Se_3$, the $(Bi_{1-x}In_x)_2Se_3$ barrier layer would behave as a metal with the TSS extending through the entire barrier layer. On the other hand, the CBM goes above the $Bi_2Se_3$ CBM when $x$ is 60%, such that the $(Bi_{1-x}In_x)_2Se_3$ layer acts as an actual potential barrier which would decouple the two TSS.
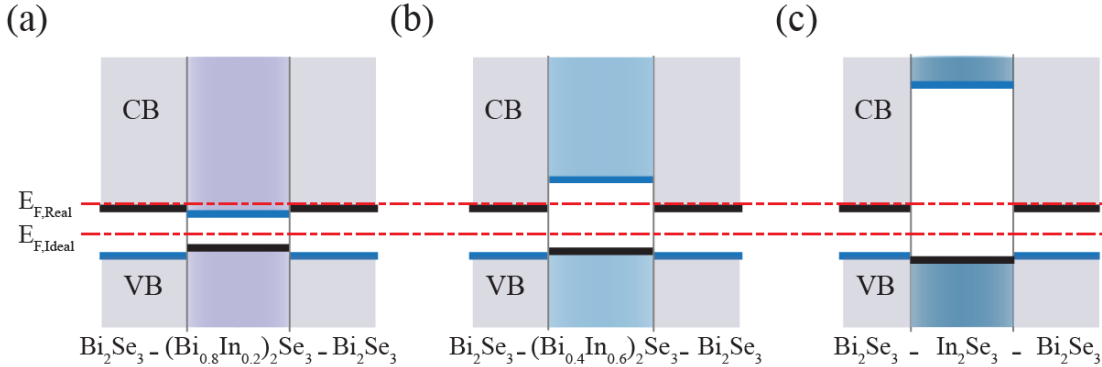


**Figure S5.** Energy bands alignment of $Bi_2Se_3$-$(Bi_{1-x}In_x)_2Se_3$-$Bi_2Se_3$ for $x = 20$, 60 and 100% respectively. For $x \gtrsim 25\%$ the conduction band minimum of $(Bi_{1-x}In_x)_2Se_3$ is above the experimental (real) Fermi level $E_{F,Real}$, which makes the barrier layer insulating, while for $x \lesssim 25\%$ the conduction band minimum drops below $E_{F,Real}$, which makes the barrier metallic: with ideal Fermi levels ($E_{F,Ideal}$), the barrier should remain insulating even for $x = 20\%$.

# C: Weak anti-localization: numerical fitting

As described in the main text, fitting the change in magneto-conductance to the HLN equation, shown in Fig. 2(a) and Fig. S6 (a-f), requires two fitting parameters, the number of conductive channels, $\tilde{A}$, which is the main focus of the main text, and the dephasing length, $l_\phi$, which is plotted in Fig. S6 (g-h) versus thickness. It can be seen that unlike $\tilde{A}$ which shows a very clear dependence on the thickness of the $(Bi_{1-x}In_x)_2Se_3$ barrier layer, $l_\phi$ shows no discernible dependence on the thickness of the barrier layer.
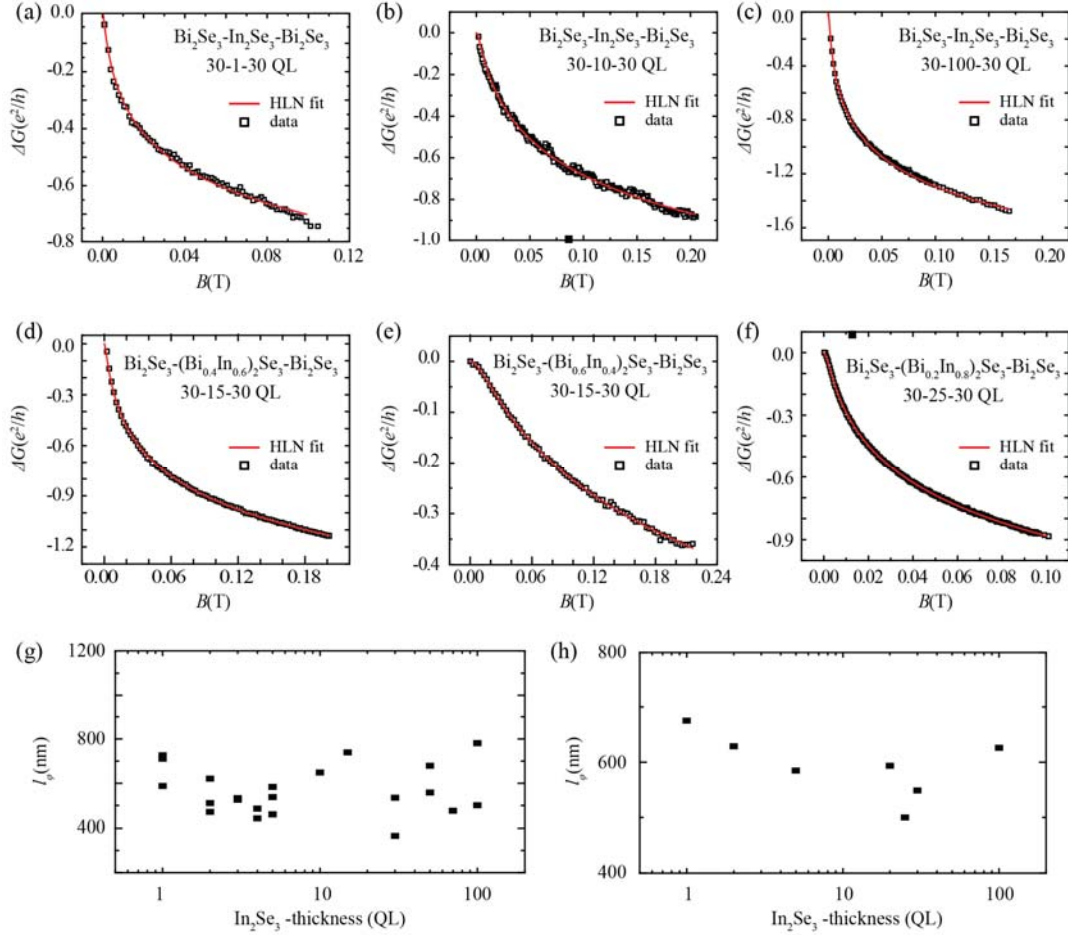


**Figure S6.** Change in conductance and numerical fits to the HLN formula for various barrier thicknesses and compositions (a-f). $l_\phi$ versus $In_2Se_3$ thickness for $Bi_2Se_3-In_2Se_3-Bi_2Se_3$ (g), and $Bi_2Se_3-In_2Se_3-Bi_2Se_3-In_2Se_3-Bi_2Se_3$ (h).

## References

[1]    H. D. Lee, C. Xu, S. M. Shubeita, M. Brahlek, N. Koirala, S. Oh, and T. Gustafsson, Thin Solid Films **556**, 322 (2014).

[2]    P. Hohenberg and W. Kohn, Phys. Rev. **136**, B864 (1964).

[3]    W. Kohn and L. J. Sham, Phys. Rev. **140**, A1133 (1965).

[4]    P. Giannozzi, S. Baroni, N. Bonini, M. Calandra, R. Car, C. Cavazzoni, D. Ceresoli, G. L. Chiarotti, M. Cococcioni, I. Dabo, A. D. Corso, S. de Gironcoli, S. Fabris, G. Fratesi, R. Gebauer, U. Gerstmann, C. Gougoussis, A. Kokalj, M. Lazzeri, L. Martin-Samos, N. Marzari, F. Mauri, R. Mazzarello, S. Paolini, A. Pasquarello, L. Paulatto, C. Sbraccia, S. Scandolo, G. Sclauzero, A. P. Seitsonen, A. Smogunov, P. Umari, and R. M. Wentzcovitch, J. Phys. Condens. Matter **21**, 395502 (2009).

[5]    J. P. Perdew, K. Burke, and M. Ernzerhof, Phys. Rev. Lett. **77**, 3865 (1996).

[6]    H. J. Monkhorst and J. D. Pack, Phys. Rev. B **13**, 5188 (1976).

[7]    N. Marzari, A. A. Mostofi, J. R. Yates, I. Souza, and D. Vanderbilt, Rev. Mod. Phys. **84**, 1419 (2012).

[8]    A. A. Mostofi, J. R. Yates, Y.-S. Lee, I. Souza, D. Vanderbilt, and N. Marzari, Comput. Phys. Commun. **178**, 685 (2008).

[9]    J. Liu and D. Vanderbilt, Phys. Rev. B **88**, 224202 (2013).

[10]   N. E. Singh-Miller and N. Marzari, Phys. Rev. B **80**, 235407 (2009).

[11]   Q. Zhang, Z. Zhang, Z. Zhu, U. Schwingenschlögl, and Y. Cui, ACS Nano **6**, 2345 (2012).

[12]   M. Brahlek, N. Bansal, N. Koirala, S.-Y. Xu, M. Neupane, C. Liu, M. Z. Hasan, and S. Oh, Phys. Rev. Lett. **109**, 186403 (2012).

[13]   L. Wu, M. Brahlek, R. Valdés Aguilar, A. V. Stier, C. M. Morris, Y. Lubashevsky, L. S. Bilbro, N. Bansal, S. Oh, and N. P. Armitage, Nat. Phys. **9**, 410 (2013).